

# The Two-Scale Radar Wave Probe and SAR Imagery of the Ocean

WILLIAM J. PLANT AND WILLIAM C. KELLER

U.S. Naval Research Laboratory, Washington, D. C. 20375

A two-scale formulation of oceanic backscatter of microwave radiation, which has previously been applied to the dual-frequency scatterometer, is applied here to the two-scale radar wave probe and SAR imagery of the ocean. A two-scale radar wave probe is a microwave system which coherently detects signals scattered from a very small patch of the ocean surface. It is shown that a SAR image may be described as a convolution of the AM part of the output of a two-scale wave probe with the power spectrum of the FM part of the output. Thus SAR images are not faithful reproductions of cross-section variations over the surface. Distortions occur as a result of variable surface velocities. Examples of this distortion are derived from two-scale wave probe data taken in the Gulf of Mexico. Application of a focusing correction does not remove the distortion from the simulated image of a nearly sinusoidal, azimuth-traveling wave. Large  $V/R_0$  ratios minimize the distortion, however.

## 1. INTRODUCTION

The observation of wave-like patterns in synthetic aperture radar (SAR) imagery of the ocean and the successful deployment of SAR aboard SEASAT have created considerable interest in the mechanisms by which SAR images the ocean. The principal feature of the ocean which complicates its imagery by SAR is its temporal variability. *Larson et al.* [1976] suggested that a distributed scatterer model was more applicable to SAR imagery of the ocean than a point target model and showed that scatterer motion, in particular, gradients of scatterer velocity, may affect the imagery. Since that time, several authors have addressed SAR imagery of the ocean using both point target and distributed scatterer models [*Jain, 1978; Swift and Wilson, 1979; Alpers and Rufenach, 1979; Valenzuela, 1980; Harger, 1980; Shuchman et al., 1981; Rufenach and Alpers, 1981; Raney, 1981; Jain, 1981; Alpers, 1982*]. The results of these efforts have not always been consistent; attempts to check their predictions against experiment are still underway [*Gonzalez et al., 1979; Beal, 1979; McLeish et al., 1980; Shuchman, 1981; Alpers et al., 1981; Beal et al., 1983*].

One convenient instrument with which SAR imagery of the ocean could be compared is the two-scale radar wave probe [*Wright et al., 1980*]. This instrument is simply a coherent microwave radar, CW or pulsed, which illuminates portions of the ocean surface that are small in comparison with dominant surface wavelengths. Several times in the past, notably during the West Coast and MARSEN experiments, such systems have been operated from stationary platforms while SAR overflights were in progress. However, comparison between the outputs of the two systems has not yet been achieved partly because of the incompletely understood relationship between the two. The aim of this paper is to lay the foundation for comparison of two-scale wave probe and SAR data. It will be shown that the two systems are not simply related through the modulation transfer function [*Wright et al., 1980*] as has been assumed by some authors. Rather, both the AM and the FM detected signals from two-scale wave probes are relevant to SAR imagery of the ocean.

An attempt will be made in this paper to hold mathematical obfuscation to a minimum. To this end, a rather simple model

of a SAR system will be employed which neglects many technical complications that are quite important in actual SAR processing. For instance, the fact that most SARs transmit chirped pulses will be disregarded and only the essential fact of high range resolution will be included in the formulation. Similarly, sampling effects will be neglected to simplify the concept. Such effects may easily be appended to the present formulation by using the methods of *Harger's* [1970] book. The reader is also referred to *Tomiyasu's* [1978] review of the subject.

In view of the fact that it is extremely difficult, if not impossible, to construct an exact mathematical model of the fluctuating ocean surface, we shall rely on a two-scale model. The structure of each scale will be represented only formally, and experimental data will be used to provide the dependence of each scale on space and time. Thus, for instance, the formulation does not restrict the class of large-scale structures to a few simple sinusoidal surface waves as has frequently been the case in the past. In principle, the large-scale structure need not even be wave-like.

Throughout this paper we assume that the radar antennas are directed at angles far enough away from nadir and grazing incidence that the composite surface model is applicable [*Wright, 1968; Bass et al., 1968*]. In section 2, output from a two-scale wave probe is modeled by using a formulation previously applied to the dual-frequency scatterometer [*Plant, 1977; Plant and Schuler, 1980*]. Some examples of field data taken with a two-scale wave probe are presented. In section 3 we apply this same formulation to SAR imagery of the ocean to show the relationship between SAR and two-scale wave probe outputs. In section 4, simulations of SAR images, using data from a two-scale radar wave probe, are presented. Finally, section 5 summarizes the results of this work.

## 2. TWO-SCALE RADAR WAVE PROBE

The theory of first-order Bragg scattering from slightly rough surfaces was first developed by *Rice* [1951]. His results for backscatter were put into a somewhat more tractable form by *Peake* [1959] and by *Wright* [1966] from whose work one may obtain the following form for the magnitude of an electromagnetic field backscattered from a slightly rough surface:

$$E(t) = B \int_{-\infty}^{\infty} \int_{-\infty}^{\infty} f_L(x', y') e^{i2k_0 R_0 g(\theta_0)} \gamma(x', y', t) \cdot e^{i2k_0 y' \cos \theta_0} dx' dy' \quad (1)$$

Copyright 1983 by the American Geophysical Union.

Paper number 3C0482.  
0148-0227/83/003C-0482\$05.00

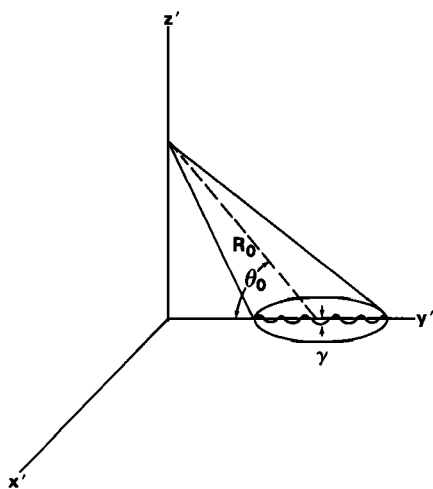


Fig. 1a

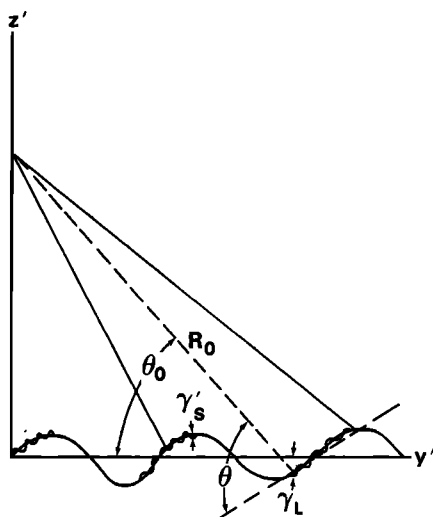


Fig. 1b

Fig. 1. (a) Geometry of slightly-rough-surface scattering. (b) Geometry of composite-surface scattering.

The coordinate system is defined in Figure 1a. In this equation,  $B$  is a function of transmitted frequency and polarization, which may be considered constant for our purposes;  $f_L$  is an illumination function defining the footprint on the surface;  $\gamma$  is the variable surface height;  $k_0$  is the transmitted wave number;  $R_0$  is the distance from the antenna to the mean surface at the center of the footprint;  $\theta_0$  is the grazing angle; and  $g(\theta_0)$  is a function of grazing angle and the electromagnetic properties of water, which is given for both polarizations by Wright [1966]. Primes on the position coordinates indicate that they are measured in a frame of reference in which the antenna is stationary.

Equation (1) says that the backscattered signal is primarily due to the Fourier component of the surface whose wave number equals the Bragg wave number,  $2k_0 \cos \theta_0$ . This equation is applicable only so long as surface slope is small and  $\gamma$  is much less than the microwavelength. The first condition is rather well satisfied by the ocean surface but the second is not. Hence, Wright [1968] and Bass et al. [1968] developed a composite surface, or two-scale, model of the scattering in which the surface height is partitioned into a large-scale dis-

placement  $\gamma_L(x', y', t)$  and a small-scale displacement  $\gamma_s'(x', y', t)$  (Figure 1b). They assumed that over any patch of the surface that is large in comparison with small-scale lengths but small when compared with large-scale lengths the scattering could be modeled as first-order Bragg scattering from the small-scale structure (i.e., they made a tangent plane approximation). Thus, the effect of  $\gamma_L$  is to change  $R$ , to tilt the surface, and to advect the small-scale structure both vertically and horizontally. If  $\gamma_L \ll y' - y_0$ , where  $y_0 = R_0 \cos \theta_0$ , expansion of the range to any point in the footprint now yields,

$$R \doteq R_0 - \gamma_L \sin \theta_0 + (y' - y_0) \cos \theta_0 + [x'^2 + (y' - y_0)^2 \sin^2 \theta] / 2R_0$$

which differs from that for a slightly rough surface by the term involving  $\gamma_L$ . The terms involving  $x'^2$  and  $(y' - y_0)^2$ , the Fresnel terms, are normally absorbed by  $f_L(x', y')$ , so, we have

$$E(t) = B \iint_{-\infty}^{\infty} f_L(x', y') g'(\theta) \gamma_s'(x', y', t) \cdot e^{-i2k_0 \gamma_L \sin \theta_0} e^{i2k_0 y' \cos \theta_0} dx' dy' \quad (2)$$

where  $\theta$  is a local grazing angle and the exponentials involving  $R_0$  and  $y_0$  are now included in  $B$ .

The function  $g'(\theta)$  differs from  $g(\theta_0)$  in (1) since  $\theta$  varies with position in the footprint. Thus, the effect of large-scale surface tilt is to introduce an effective amplitude modulation of the small-scale structure through  $g'(\theta)$ . In addition to this, small-scale structure is known to be amplitude modulated by velocities associated with large-scale structure. We model all these amplitude-modulating influences by a function  $h(x', y', t)$ , which has scale lengths characteristic of the large-scale structure. Thus, we have

$$E(t) = B \iint_{-\infty}^{\infty} f_L(x', y') h(x', y', t) \cdot e^{-i2k_0 \gamma_L \sin \theta_0} \gamma_s(x', y', t) e^{i2k_0 y' \cos \theta_0} dx' dy' \quad (3)$$

Here,  $\gamma_s$  differs from the true small-scale displacement  $\gamma_s'$  in that the amplitude-modulating influence of the large-scale structure has been removed. Thus, the mean square value of  $\gamma_s$  is the same everywhere on the surface. Influence of the large-scale structure on the frequency content of  $\gamma_s'$  remains in  $\gamma_s$ , however. This influence is expressed by the relationship between the frequency of a wave advected by a current as measured in frames of reference which are stationary and moving at the current velocity. Thus, the frequency  $f$  of a small-scale wave measured in the antenna's frame of reference is

$$f = f_0 + \mathbf{k} \cdot \mathbf{U}(x', y', t) / 2\pi \quad (4)$$

where  $\mathbf{k}$  is the small wave number,  $\mathbf{U}$  is the large-scale surface velocity, and  $f_0$  is the frequency of the small-scale wave in a frame of reference moving with the current. Both  $\gamma_s$  and  $h$  are random functions and, to a good approximation, are uncorrelated; we shall also assume that they are statistically independent. We mention in passing that if  $\gamma_L$  is not sufficiently small when compared with  $(y' - y_0)$ , then  $f_L(x', y')$  may also contain modulations due to the large-scale structure. In practice, these modulations are small and can be included in  $h(x', y', t)$  so that  $f_L$  need not be considered time dependent.

Equation (3) has been successfully employed in the past to explain backscattered sea return to dual-frequency scatterome-

ters [Plant, 1977; Plant and Schuler, 1980]. Here we apply it to backscattered sea return to a two-scale radar wave probe that is stationary on earth. Thus we let both dimensions of the footprint be small in comparison with large-scale structure but large when compared with small-scale structure. To indicate this special case, we change the notation of  $f_L$  to  $f_s$ . The field  $E(t)$ , then, is parametrically dependent on the coordinates  $(x_0, y_0)$  of the center of the illuminated spot. We may approximate the integral in (3) by replacing  $h$  by its mean value over the illuminated area to get

$$E(t) = Bh(x_0, y_0, t) \iint_{-\infty}^{\infty} f_s(x, y) \cdot e^{-i2k_0\gamma_L \sin\theta_0} \gamma_s(x, y, t) e^{i2k_0y \cos\theta_0} dx dy \quad (5)$$

We have dropped the primes in this equation since primed and unprimed coordinates are identical in this case.

Consider now the power spectrum  $P(f)$  of the field  $E(t)$  computed during a time interval centered at  $t = t_0$ . We have

$$P(f) = B^2 \left| \int_{-\infty}^{\infty} f_T(t) [h(x_0, y_0, t) e^{i2k_0\gamma_L} \iint_{-\infty}^{\infty} f_s(x, y) \cdot e^{-2k_0\gamma_L \sin\theta_0} \gamma_s(x, y, t) e^{i2k_0y \cos\theta_0} dx dy] e^{-i2\pi f t} dt \right|^2 \quad (6)$$

where  $f_T(t)$  is a temporal window function of width  $T$  and  $P(f)$  is parametrically dependent on  $x_0, y_0$ , and  $t_0$ . Assuming that all functions are well behaved at infinity, we may carry out the squaring operation to get

$$P(f) = B^2 \langle |h(x_0, y_0, t_0)|^2 \rangle \iiint_{-\infty}^{\infty} R(q, p, \tau) \cdot e^{-i2k_0\rho \cos\theta_0} e^{i2\pi f \tau} dq dp d\tau \quad (7)$$

where  $R$  is the small-scale autocorrelation function, the angle brackets represent the time integral over the window  $T$ , and we have made use of the statistical independence of  $h$  and  $\gamma_s$ . In obtaining this equation, we have assumed that the small-scale autocorrelation function,

$$R(q, p, \tau) = \iint_{-\infty}^{\infty} \langle e^{-i2k_0(\gamma_L - \gamma_L^*) \sin\theta_0} \gamma_s(x, y, t) \cdot \gamma_s^*(x+q, y+p, t+\tau) \rangle |f_s(x, y)|^2 dx dy \quad (8)$$

falls to zero sufficiently rapidly as  $\rho, q$ , or  $\tau$  increases that the values of these variables can be approximated by zero in the large-scale function  $h$ . In (8)  $\gamma_L$  is evaluated at  $(x, y, t)$ , while  $\gamma_L^*$  is evaluated at  $(x+q, y+p, t+\tau)$ .

The assumption that  $R(q, p, \tau)$  falls to zero for values of its argument which are much smaller than large-scale wavelength or period parameters is based on an accumulation of experimental evidence over many years. A large amount of data exists to indicate that Doppler spectra of microwave sea return have widths from a few tens of Hertz to a few hundred Hertz depending on frequency [see, for instance, Valenzuela and Laing, 1970]. Since the inverse of these frequencies yield decorrelation times, these measurements imply decorrelation times of 10–100 ms, much smaller than dominant wave periods. Figure 3 below also confirms this fact. Pidgeon [1967] showed that spatial

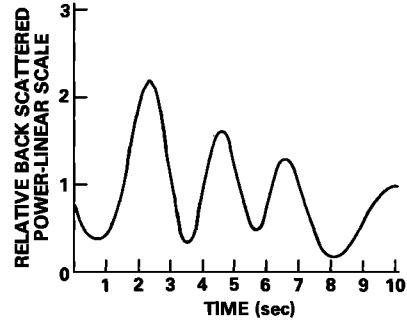


Fig. 2. Relative power backscattered to an X band, two-scale, radar wave probe as a function of time. The grazing angle was  $45^\circ$ , and a  $2.5 \text{ m} \times 3.3 \text{ m}$  spot was illuminated on the surface. The data have been low-pass filtered at 0.5 Hz.

decorrelation of backscattered sea return at low angles occurs when illuminated areas are separated by more than their width. He used widths down to 15 m, so his results imply a spatial decorrelation length for the small-scale structure that is smaller than this value. Furthermore, video measurements in the Gulf of Mexico by Gotwols and Irani [1980] indicate that 1.5 Hz waves decorrelate in a distance of 1–2 m. The trend of their data indicates that this number decreases with increasing wave frequency. Finally, the output of a dual-frequency scatterometer is well explained on the basis of rapid temporal and spatial decorrelation of small wave structure [Alpers and Hasselmann, 1978; Plant and Schuler, 1980].

Let us define the power spectrum of the small-scale structure  $\gamma_s$  to be

$$\psi(f) = \iiint_{-\infty}^{\infty} R(q, \rho, \tau) e^{-i2k_0\rho \cos\theta_0} e^{i2\pi f \tau} dq dp d\tau \quad (9)$$

If the length  $T$  of the temporal window  $f_T$  is small, this function is parametrically dependent on  $x_0, y_0$ , and  $t_0$  through  $\gamma_L$  and the dependence of  $f$  on these parameters as given by (4). Using (9), we may write (7) in the form

$$P(f) = B^2 \langle |h(x_0, y_0, t_0)|^2 \rangle \psi(f) \quad (10)$$

We see that  $\langle |h|^2 \rangle$  is proportional to the integral of  $P(f)$  over small-scale frequencies (i.e., to the power or cross-section fluctuations introduced in the backscattered signal by the large-scale structure). Plant and Schuler [1980] have related  $\langle |h|^2 \rangle$ , which they called  $H$ , to the modulation transfer function and long wave slope for the case where the horizontal antenna direction is parallel to the wave propagation direction. If large-scale homogeneity exists,  $\langle |h|^2 \rangle$  must become independent of  $x_0, y_0$ , and  $t_0$  for long time windows  $T$ , but will be parametrically dependent on  $x_0, y_0$ , and  $t_0$  for short time windows.

In practice,  $\langle |h|^2 \rangle$  is more easily determined for short  $T$  by squaring  $E(t)$  and filtering out small-scale frequencies. Figure 2 is an example of these large-scale power fluctuations obtained with a two-scale, CW, X band wave probe operated in the Gulf of Mexico. The data were taken on December 4, 1978, from an offshore tower, stage I, operated by the Naval Coastal Systems Center. The tower is located 12 miles from the Florida coast in 32 m of water. Wind speed, measured 22 m above the mean surface level, was 11.5 m/s, and the microwave antenna, mounted 20 m above mean water level, was pointed into the wind. Air temperature was  $24.0^\circ\text{C}$ , while water temperature was  $22.4^\circ\text{C}$ . The antenna was set at a  $45^\circ$  grazing angle, vertical

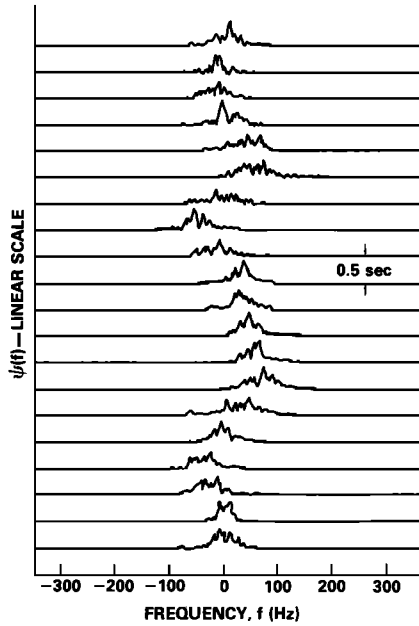


Fig. 3. Power spectrum of the clipped signal from an X band, two-scale, radar wave probe versus time. Each trace is the power spectrum of a 0.5-s time record as a function of frequency. Successively lower traces correspond to successively later 0.5-s time intervals. The same data were used to produce Figures 2 and 3;  $t = 0$  in Figure 2 corresponds to the top trace here.

polarization was used, and the surface area illuminated was approximately 2.5 by 3.3 m. The return signal has been squared and low-pass filtered at 0.5 Hz. The vertical scale is relative since absolute power was not measured.

Since all large-scale amplitude variation in  $E(t)$  is contained in  $h$ , we may observe a signal proportional to  $\psi$  by clipping  $E(t)$  and computing the power spectrum over times  $T$  intermediate between small- and large-scale times. Figure 3 shows the results of such operations for the same data that was used to produce Figure 2. The individual sweeps shown in Figure 3 are power spectra of the clipped signal computed in successive 0.5 s time intervals. The influence of variable, large-scale surface velocities on small-scale frequencies is clearly seen in the shift of the mean spectral frequency with time. Note that the bandwidths of these spectra imply decorrelation times of about 10–20 ms. Figures 2 and 3 are synchronized with  $t = 0$  in Figure 2 corresponding to the top sweep in Figure 3. Later times are lower sweeps in Figure 3. Once again, vertical scales represent only relative intensities.

Figures 2 and 3 illustrate the reason for calling this type of system a two-scale wave probe. The function  $\langle |h|^2 \rangle$  is primarily due to amplitude modulation of the small-scale structure [Wright et al., 1980]. Thus information on small-scale waves is contained in this function. On the other hand, the mean frequency of any spectrum  $\psi(f)$  is determined by large-scale velocities as given by (4). Thus computing  $\psi(f)$  in successive short time intervals yields large-scale surface velocity as a function of time [Plant et al., 1978].

### 3. SAR IMAGERY OF THE OCEAN

We now apply (3) to SAR imagery of the ocean. The geometry of the situation is illustrated in Figure 4. The antenna is carried in an aircraft or spacecraft moving with speed  $V$  in the  $x$  direction. The antenna footprint is large when compared with large-scale structure in the  $x$  direction but small when com-

pared with large-scale lengths in the  $y$  direction. Because of the platform motion, scatterers that are stationary in the earth-fixed frame of reference exhibit a Doppler shift in the antenna's frame of reference over portions of the footprint which do not coincide with the  $y$  axis. This effect is included in (3) through the Fresnel terms that were absorbed in  $f_L(x', y')$ . To write (3) in a frame of reference fixed on earth, we must let

$$\begin{aligned} y' &= y \\ x' &= x - Vt \end{aligned} \tag{10}$$

where unprimed variables are measured in the earth-fixed reference frame. Then, the Fresnel term involving  $x'^2$  becomes

$$e^{ik_0 x'^2/R_0} = e^{ik_0(x^2 - 2Vxt + V^2t^2)/R_0} \tag{11}$$

Absorbing the  $x^2$  term in  $f_L$ , (3) written in the earth-fixed reference frame is

$$\begin{aligned} E(t) &= B e^{ik_0 V^2 t^2 / R_0} \iint_{-\infty}^{\infty} f_L(x, y, t) h(x, y, t) \\ &\cdot e^{-i2k_0 \gamma_L \sin \theta_0 y} \gamma_s(x, y, t) e^{i2k_0 y \cos \theta_0} \\ &\cdot e^{-i2k_0 V x t / R_0} dx dy \end{aligned} \tag{12}$$

where  $f_L$  is now time-dependent because the footprint sweeps across the ocean surface. This function produces an effective time window of width  $L/V$  where  $L$  is the distance illuminated in the  $x$  direction. This is just the time during which any point of the surface is illuminated by the moving footprint. Below we shall impose a second time window of width  $T$  centered at  $t_0$  during SAR processing. Typically,

$$T < L/V \tag{13}$$

so that the larger window is irrelevant in most cases. Thus we shall let  $t = t_0$  when evaluating  $f_L$  in the following development.

Now, the large spatial extent of  $f_L$  in the  $x$  direction can be represented as a sum of small footprints  $f_s$  with  $s = 1$  to  $N$ . Then, coordinates at the center of the  $s$ th footprint are  $(x_s - Vt_0, y_0)$  and

$$E(t) = B e^{ik_0 V^2 t^2 / R_0} \sum_{s=1}^N h(x_s, y_0, t)$$

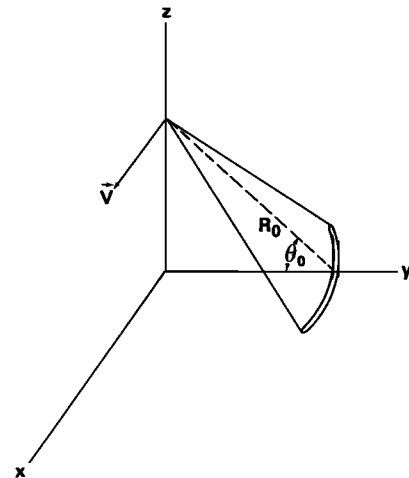


Fig. 4. Geometry of SAR scattering.

$$\cdot \iint_{-\infty}^{\infty} f_s(x, y) e^{-i2k_0 \gamma_L \sin \theta_0 \gamma_s(x, y, t)} \cdot e^{i2k_0 y \cos \theta_0} e^{-i2k_0 V x t / R_0} dx dy \quad (14)$$

where  $h(x_s, y_0, t)$  refers to the mean value of this large-scale quantity over the small footprint.

SAR processing consists essentially of multiplying  $E(t)$  by a focusing term  $\exp(-iat^2)$ , Fourier transforming, and taking the magnitude squared. The result is a SAR image  $I(x_0, y_0)$  of the scene which is given by

$$I(x_0, y_0) = B^2 \left| \sum_{s=1}^N \int_{-\infty}^{\infty} \left\{ f_T(t) h(x_s, y_0, t) \cdot \iint_{-\infty}^{\infty} f_s(x, y) e^{-i2k_0 \gamma_L \sin \theta_0 \gamma_s(x, y, t)} \cdot e^{i2k_0 y \cos \theta_0} e^{i2k_0 V(x_0 - x)t/R_0} dx dy \right\} dt \right|^2 \quad (15)$$

where we have set

$$a = k_0 V^2 / R_0 \quad (16)$$

Here we have represented the frequency of the Fourier transform by  $k_0 V x_0 / R_0 \pi$  since this frequency determines the  $x$  coordinate in the SAR image of a stationary object. Once again,  $f_T$  is a time window of width  $T$ .

As in section 2, we now carry out the squaring operation assuming that the small-scale autocoherecence function is a narrow function of lag variables so that these variables may be ignored in the large-scale quantity  $h$ . The result is

$$I(x_0, y_0) = B^2 \sum_{s=1}^N \langle |h(x_s, y_0, t_0)|^2 \rangle \iiint_{-\infty}^{\infty} \iiint_{-\infty}^{\infty} |f_s(x, y)|^2 \cdot \langle e^{-i2k_0(\gamma_L - \gamma_L^*) \sin \theta_0 \gamma_s(x, y, t)} \gamma_s^* \cdot (x + q, y + \rho, t + \tau) e^{-i2k_0 V(t + \tau)q/R_0} \cdot e^{-2k_0 \rho \cos \theta_0} e^{i2k_0 V(x_0 - x)\tau/R_0} dx dy d\rho dq d\tau \quad (17)$$

where the summation was taken outside of the square due to the rapid decay of the small-scale autocoherecence function with  $q$ ,  $\rho$ , and  $\tau$ . Here,  $t_0$  is the time at the center of the temporal interval over which the Fourier transform is taken. Since time is related to the  $x$  dimension through the platform velocity, we may write,

$$t_0 = x_0 / V \quad (18)$$

Consider now the transform variable of  $q$ . Call it  $k_x$  where

$$k_x = \frac{2k_0 V(t + \tau)}{R_0} \quad (19)$$

Since  $\tau$  is small, the maximum value of  $V(t + \tau)/R_0$  is approximately  $VT/R_0$ . Typically, this is sufficiently small that

$$k_x \ll 2k_0 \cos \theta_0 \quad (20)$$

for grazing angles away from nadir. Thus we may let  $k_x = 0$  with little error. In fact, similar approximations for  $k_x$  are inherent in (1).

A similar argument shows that the term

$$e^{i[2k_0 V(x_0 - x)/R_0]\tau}$$

must vary slowly over  $x$  so that we may let  $x = x_s$  in the exponent. Then we have

$$I(x_0, y_0) = B^2 \sum_{s=1}^N \langle |h(x_s, y_0)|^2 \rangle \psi(x_0 - x_s) \quad (21)$$

where

$$\psi(x_0 - x_s) = \iiint_{-\infty}^{\infty} R(q, \rho, \tau) \cdot e^{-i2k_0 \rho \cos \theta_0} e^{i[2k_0 V(x_0 - x_s)/R_0]\tau} d\rho dq d\tau \quad (22)$$

with  $R$  given by (8). This is precisely the same as  $\psi$  defined in section 2 for the two-scale wave probe if

$$f = \frac{k_0 V(x_0 - x_s)}{\pi R_0} \quad (23)$$

Equation (21) is strictly correct only if  $f_s$  is sufficiently narrow in the  $x$  direction that the resolution is determined by the temporal window rather than by the width of  $f_s$ . In this limit, the sum in (21) becomes an integral and the equation may be written somewhat more perspicuously,

$$I(x_0, y_0) = \frac{B^2}{\Delta x_s} \int_{-\infty}^{\infty} f_L(x_s) \langle |h(x_s, y_0)|^2 \rangle \psi(x_0 - x_s) dx_s \quad (24)$$

where  $\Delta x_s$  corresponds to the very narrow width of  $f_s$  in the  $x$  direction. Note that  $f_L(x_s)$  is centered at  $x_0$  and is parametrically dependent on  $y_0$ . Similarly,  $\psi(x_0 - x_s)$  depends on  $x_0$  and  $y_0$  in addition to its dependence on  $x_0 - x_s$ .

Equations (23) and (24) are the connection which we have sought between a SAR image and the output of a two-scale wave probe. To see their significance, suppose that the scene being imaged is independent of time (i.e.,  $h$  and  $\gamma_s$  vary only spatially). Then the integral over  $\tau$  in (22) for sufficiently long temporal windows  $T$  yields

$$\psi(x_0 - x_s) \propto \delta(x_0 - x_s) \quad (25)$$

Thus, (24) yields

$$I(x_0, y_0) \propto \langle |h(x_0, y_0)|^2 \rangle \quad (26)$$

and the SAR image is a faithful representation of surface cross section. Azimuthal resolution of the SAR may be found in this case by using (23) which implies that

$$\Delta f = \frac{2V \Delta x}{\lambda R_0} \quad (27)$$

where  $\lambda = 2\pi/k_0$  is the microwavelength. But  $\Delta f = T^{-1}$  so the SAR resolution in the  $x$  direction is given for stationary targets by

$$\Delta x = \frac{\lambda R_0}{2TV} \quad (28)$$

as usual [Harger, 1970].

Evaluation of the integral in (24) may be represented schematically for this case as shown in Figure 5. The  $\delta$  function is shown at various values of  $x_0$  in the skewed, falling-raster display at the top of the figure. The function  $\langle |h|^2 \rangle$  is shown as a function of  $x_s$  just below the raster display. The integral consists of multiplying the  $\delta$  function trace, which is offset by a amount  $x_0$ , point by point with the trace of  $\langle |h|^2 \rangle$  and integrating over  $x_s$ . This yields  $I(x_0, y_0)$  for that particular value of

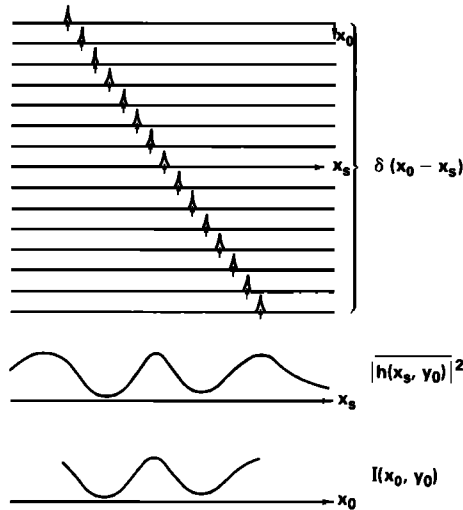


Fig. 5. Pictorial illustration of the convolution of (24) for the case of stationary scatterers. Arrows represent points where  $x_s = x_0$ . The image  $I$  is a reproduction of cross-section variation,  $\langle |h|^2 \rangle$ .

$x_0$ . As shown in (26) and the bottom of Figure 5, if  $x_0$  is varied, the result is just reproduction of  $\langle |h|^2 \rangle$ .

Consider, however, the case of oceanic imagery where both  $h$  and  $\gamma_s$  vary with time. If we assume all large-scale structure to be due to surface waves with a sharp spectrum, then we may infer  $\psi(x_0 - x_s)$  from  $\psi(f)$  as shown in Figure 3. The top part of Figure 6 shows a schematic representation of  $\psi(f)$  similar to that of Figure 3 except that now we consider successively lower traces to be at different positions  $x_s$ . Then (22) requires that we evaluate  $\psi(f)$  along the line given by (23) in order to obtain  $\psi(x_0 - x_s)$ . Three such diagonal lines, corresponding to three different values of  $x_0$ , are shown in the top part of Figure 6. We obtain  $\psi(x_0 - x_s)$  from the value of  $\psi(f)$  at intersections of diagonal and horizontal lines. For instance, the middle diagonal line crosses the seventh horizontal line from the bottom at  $f = 0$ . Thus this point corresponds to  $x_0 = x_s$  and this diagonal line yields the seventh horizontal line from the bottom in the central part of the figure. Note that  $\psi(x_0 - x_s)$  is zero where  $x_0 = x_s$  on the horizontal line because  $\psi(f)$  was zero at the diagonal-horizontal intersection in the top part of the figure. Similarly, the region on this horizontal line where  $\psi(x_0 - x_s)$  is not zero and  $x_s < x_0$  arises due to the diagonal line cutting through regions where  $\psi(f) \neq 0$  in the upper part of this figure.

The function  $\psi(x_0 - x_s)$  is represented in the central part of Figure 6 for various  $x_0$  values in a skewed, falling-raster display similar to that used to depict  $\delta(x_0 - x_s)$  in Figure 5. Indeed, if  $\psi(f) = \delta(f - f_0)$  then  $\psi(x_0 - x_s) = \delta(x_0 - x_s)$  as before. It is  $\psi(x_0 - x_s)$  which is now convolved with  $\langle |h|^2 \rangle$  as  $\delta(x_s - x_0)$  was in Figure 5 to produce the SAR image of the ocean shown at the bottom of the figure. Note that  $\psi(x_0 - x_s)$  is not always centered at  $x_s = x_0$ , nor is it of constant width. In fact, the slope of the  $f$  versus  $x_s$  line depends on  $V/R_0$  and, for small  $V/R_0$ , may intersect  $\psi(f)$  at several different values of  $x_s$ . (Note the lowest diagonal line.) Thus,  $\psi(x_0 - x_s)$  is not necessarily localized near  $x_0$  for large surface velocities or small  $V/R_0$  ratios. The distortion of  $\psi(f)$  to obtain  $\psi(x_0 - x_s)$  is a direct result of large-scale current gradients on the ocean surface; in the case of ocean waves these current gradients are the orbital velocity gradients. Steady currents would only displace  $\psi(x_0 - x_s)$  from  $x_s = x_0$  by a constant amount and would not affect its shape.

Distortions of the image thus occur as a result of large-scale current gradients as indicated in Figure 6. Larson et al. [1976]

have noted that this distortion makes it possible for an SAR to image current gradients even if  $\langle |h|^2 \rangle$  is constant. The size of this effect, of course, depends on the magnitude of the gradients. Figure 3 indicates that  $\psi(f)$  at X band may be displaced from zero by as much as 100 Hz by ocean surface waves. For  $V/R_0 = 0.01$  and  $k_0 = 2 \text{ cm}^{-1}$ , appropriate for an X band radar, (23) yields a position displacement of about 150 m for  $f = 100 \text{ Hz}$ . Clearly, this is a nonnegligible effect. Note that the maximum frequency shift is proportional to  $k_0$ , so the position displacement will be independent of radar frequency. Azimuthal resolution in this case is still determined from (27) where  $\Delta f$  is the width  $\psi(f)$  of Figure 6 and  $\Delta x$  is the width of  $\psi(x_0 - x_s)$ . Now, however,  $\psi(x_0 - x_s)$  is not necessarily narrow, of constant width, or single peaked.

To relate this formulation to previous work on SAR imagery of ocean waves, let us consider for the moment the case where a single sinusoidal wave exists on the surface. Thus, large-scale surface height is

$$\gamma_L = A \cos(\mathbf{K} \cdot \mathbf{x} - \Omega t) \quad (29)$$

and the line-of-sight velocity observed by the radar wave probe is

$$v(x, y, t) = \Omega A (\sin^2 \theta_0 \tanh^2 Kd + \cos^2 \phi \cos^2 \theta_0)^{1/2} \cos(\mathbf{K} \cdot \mathbf{x} - \Omega t + \phi_D) \quad (30)$$

where

$$\phi_D = \tan^{-1} \left( \frac{\tanh Kd \tan \theta_0}{\cos \phi} \right) \quad (31)$$

$\mathbf{K}$  is long-wave number,  $\Omega$  is its frequency,  $d$  is water depth, and  $\phi$  is the angle between  $\mathbf{K}$  and the horizontal antenna-look direction. Then,  $\langle |h|^2 \rangle$  will be given by

$$\langle |h(x, y, t)|^2 \rangle = P_0 [1 + m(KA) \cos(\mathbf{K} \cdot \mathbf{x} - \Omega t + \phi_m)] \quad (32)$$

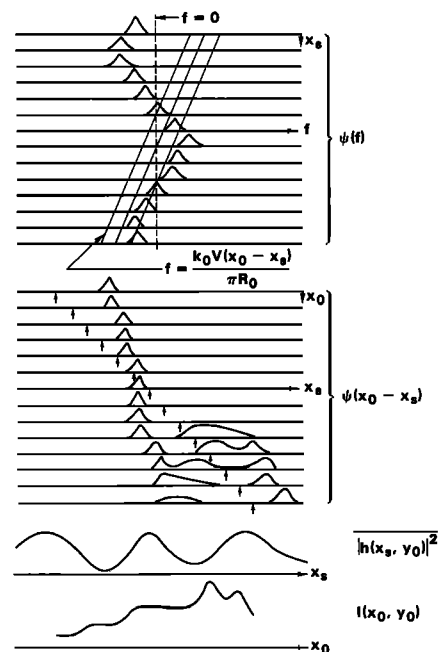


Fig. 6. Pictorial illustration of the convolution of (24) for the case of oceanic scattering.  $\psi(x_0 - x_s)$  is obtained by evaluating  $\psi(f)$  at intersections of horizontal and diagonal lines in the top part of the figure. Arrows represent points where  $x_s = x_0$ . The image  $I$  is no longer a reproduction of cross-section variation,  $\langle |h|^2 \rangle$ .

where  $m$  is the magnitude of the modulation transfer function including both tilt and hydrodynamic modulation,  $\phi_m$  is its phase, and  $P_0$  is the mean scattered power.

If the width of  $\psi(f)$  is narrow enough to be considered a  $\delta$  function, then we may write for this case

$$\psi(f) = \delta(f - k_0 v(x_s, y_0, t)/\pi) \quad (33)$$

Thus, using (23),  $\psi(x_0 - x_s)$  is given by

$$\psi(x_0 - x_s) = \frac{\pi R_0}{k_0 V} \left( 1 - \frac{R_0}{V} \frac{\partial v}{\partial x_s} \right) \delta(x_0 - x_s) \quad (34)$$

where we have assumed that

$$\frac{R_0}{V} \left( \frac{\partial v}{\partial x_s} \right)_{\max} \ll 1 \quad (35)$$

Note that this is simply the condition that the slope  $|df/dx_s|$  of the diagonal lines in Figure 6 is greater than the maximum rate of change of the center of  $\psi(f)$  with  $x_s$  (i.e., that  $\psi(f)$  is appreciable at only one intersection of horizontal and diagonal lines). It is also the linearity condition given by *Alpers et al.* [1981] under which SAR images are linearly related to long ocean wave height. We may obtain this linear relationship by substituting (32) and (34) into (24) and assuming that  $f_L(x_s)$  is very broad:

$$I(x_0, y_0) = \frac{B^2 P_0 \pi R_0}{\Delta x_s K_0 V} \left\{ 1 + [R_0 \Omega K A \cos \phi_x (\sin^2 \theta_0 \tanh^2 K d + \cos^2 \phi \cos^2 \theta_0)^{1/2} / V] \{ \sin(\mathbf{K} \cdot \mathbf{x}_0 - \Omega t_0 + \phi_D) + m K A \cos \mathbf{K} \cdot \mathbf{x}_0 - \Omega t_0 + \phi_m \} \right\} \quad (36)$$

where  $t_0$  is given by (18) and  $\phi_x$  is the angle between  $\mathbf{x}_0$  and  $\mathbf{K}$ . This expression agrees with the result of *Alpers et al.*; the second term is their velocity-bunching expression.

If  $x_0/V$  is substituted into (36) for  $t_0$ , we see that the wavelength of the wave in the image will be

$$\mathbf{K}_{\text{image}} = (K \cos \phi_x - \Omega/V) \hat{a}_x + K \sin \phi_x \hat{a}_y \quad (37)$$

where  $\hat{a}_x$  and  $\hat{a}_y$  are unit vectors. Thus, for  $\phi_x < 90^\circ$ , the wave number of the image wave is smaller than that of the surface wave and the propagation direction is rotated toward the range direction. This agrees with results of previous authors [*Valenzuela*, 1980; *Harger*, 1980].

So far we have considered only the case where the focusing procedure used during SAR processing was adjusted for stationary targets. One focusing adjustment that can be made during processing is to vary the parameter 'a' from the value given by (16). Optically, this is accomplished by varying the position of a lens along the optical bench. Formally, this adjustment amounts to a multiplication of  $\gamma_s$  by a quadratic exponential term; that is, to making the following substitution in previous equations for  $I(x_0, y_0)$ :

$$\gamma_s \rightarrow e^{-i\Delta a t^2} \gamma_s \quad (38)$$

where

$$\Delta a = \frac{2k_0 V \Delta V}{R_0} \quad (39)$$

In the simulation of SAR imagery from two-scale radar wave probe data, this change is accomplished simply by multiplying the clipped signal by  $\exp(-i\Delta a t^2)$ .

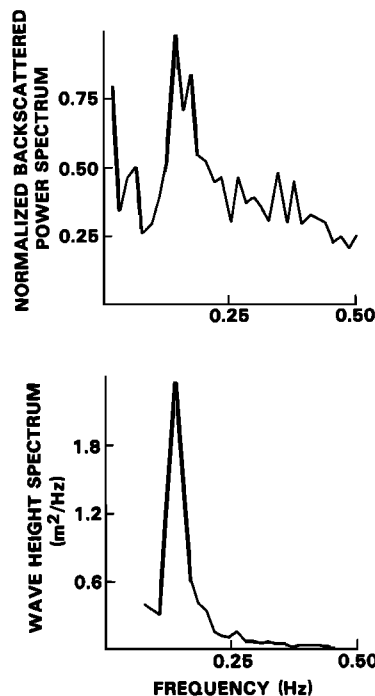


Fig. 7. (a) Normalized power spectrum of  $\langle |h|^2 \rangle$  for the radar wave probe data used in SAR image simulation. (b) Power spectrum of wave heights obtained from the FM part of the radar wave probe output used in simulation.

#### 4. SIMULATED SAR IMAGERY

To apply (24) in a strictly correct manner to the simulation of SAR imagery, one would need an array of two-scale probes spaced along the  $x$  and  $y$  axes. Since this is impractical, we shall assume in this section that the ocean wave spectrum is sufficiently narrow that we can infer the wave spatial distribution from the time record. This approximation should be rather good for times up to the inverse of the width of the wave height spectrum.

Data used in the following simulation were obtained on November 30, 1978, by using the X band radar wave probe in the Gulf of Mexico. Antenna parameters were as described in section 2. In the present case, however, the antenna-look direction made an angle of  $85^\circ$  with the wind and wave direction. Wind speed was 5.6 m/s, air temperature was  $19.6^\circ\text{C}$ , and water temperature was  $21.7^\circ\text{C}$ . Figure 7a shows the spectrum of the backscattered power received by the system (i.e., the power spectrum of  $\langle |h|^2 \rangle$ ). Figure 7b shows the wave height spectrum obtained from the FM part of the received signal. Previous studies have shown this to correspond well to spectra produced by point probes [*Plant et al.*, 1983]. From these two spectra, we infer that variations in received power follow the surface wave slope fairly well in this case. The peak frequency of 0.14 Hz corresponds to a dominant wavelength of 80 m.

The simulation procedure was implemented on our laboratory computer, a Digital Equipment Corporation MNC11-CA containing an LSI 11/23 processor and 256 kilobytes of memory. The program assumed that three dominant wavelengths were contained in the SAR footprint in the azimuthal direction. Variation of this number up to 12 dominant wavelengths did not affect the image. Integration time,  $V/R$  ratios, and  $\Delta V$ , the focusing parameter, were all variable. Raw radar wave probe data beat down to audio frequencies were digitized, squared, and averaged over the integration time to obtain  $\langle |h(x_s)|^2 \rangle$ . To obtain  $\psi(f)$ , the raw data were first clipped then

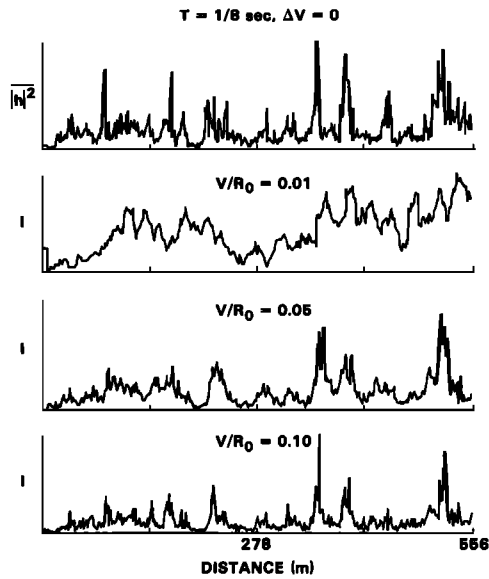


Fig. 8. Relative cross section  $\langle |h|^2 \rangle$  and simulated SAR images  $I$  versus position for various  $V/R_0$  ratios.  $T = 1/8$  s,  $\Delta V = 0$ . Vertical scales are linear.

multiplied by the quadratic exponential term involving  $\Delta a$ . Power spectra of this time record over times equal to the integration time were computed and used to obtain  $\psi(x_0 - x_s)$  as illustrated in Figure 6. The distance between the discrete  $x_s$  values was taken to be the dominant wave phase speed times the integration time. Finally,  $I(x_0, y_0)$  was computed by integrating the product of  $\langle |h(x_s)|^2 \rangle$  and  $\psi(x_0 - x_s)$  over all  $x_s$  values within the SAR footprint. In these computations it was assumed that the platform velocity was large when compared with the wave phase speed. Only single-look processing may be simulated by this method.

Figures 8–10 show the results of this simulation for several different combinations of parameters. In all three figures, the top curve shows the cross section variation along the line  $y = y_0$  as inferred from the radar wave probe temporal record; the same 50-s time record was used in all cases. All figures indicate some degree of distortion in the image when compared with the cross-section trace. While such distortion was never

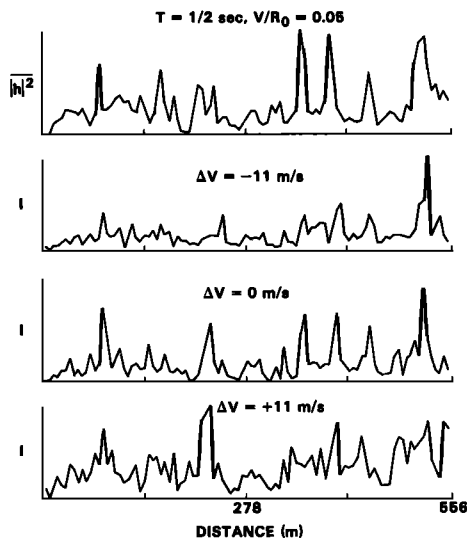


Fig. 9. Relative cross section  $\langle |h|^2 \rangle$  and simulated SAR images  $I$  versus position for various focusing parameters  $\Delta V$ .  $T = 1/2$  s,  $V/R_0 = 0.05$ . Vertical scales are linear.

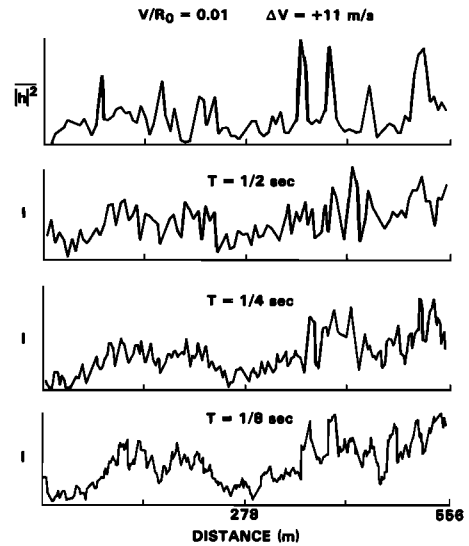


Fig. 10. Relative cross section  $\langle |h|^2 \rangle$  and simulated SAR images  $I$  versus position for various integration times  $T$ .  $V/R_0 = 0.01$ ,  $\Delta V = +11$  m/s. Vertical scales are linear.

completely removed, it was significantly reduced by increasing the ratio  $V/R_0$ . Figure 8 gives an example of this effect. The images formed with  $V/R_0 = 0.05$  and  $0.10$  more nearly reflect cross-section changes than does the image formed with  $V/R = 0.01$ .

Variation of the focusing parameter  $\Delta V$  produced the most effect when integration times were relatively long and  $V/R_0$  was large. Figure 9 shows the change in the image in one such case when  $\Delta V$  was adjusted over a range comparable to the dominant wave phase speed. The parameters used in this case imply that the stationary-target resolution limit is the spot size of the radar wave probe and not the integration time. Thus, ideal conditions for simulation are not well met. Widths of the  $\psi(f)$  spectra, however, imply that the stationary-target resolution is not approached in this case. Thus, the simulated image should be rather good.

Finally, the simulation indicates that the integration time can have a dramatic effect on the shape of the image. This is indicated in Figure 10 where the image distortion clearly depends on integration time. For instance, the peak in the  $T = 1/8$ -s image near 470 m is completely absent from the  $T = 1/2$ -s image in Figure 10. This presumably results from a change in  $\psi(f)$  over the two integration periods since  $\langle |h|^2 \rangle$  does not differ in the two cases as the top traces in Figs. 8 and 9 show.

### 5. CONCLUSION

This work has related SAR imagery of the ocean to the output of two-scale radar wave probes. The relationship is expressed by (23) and (24); the SAR image is a convolution of the AM part of the radar wave probe output with the power spectrum of the FM part. This, of course, requires that the antenna of the two radar systems point in the same direction. Differences between image formation of oceanic scenes and stationary scenes result from differences in the spectrum of the FM part of the signal over the integration time (i.e., differences in  $\psi(f)$ ). The two cases are described following (24) and are illustrated in Figures 5 and 6. For stationary scenes,  $\psi(f)$  is very narrow with a width determined by the integration time and centered at a constant frequency. For ocean scenes,  $\psi(f)$  is

broad and exhibits a time-dependent mean. The broadening of  $\psi(f)$  by itself would simply degrade the azimuthal resolution of the image. The shifting mean frequency, however, causes distortion of the image which cannot be removed. The position of the center of the spectrum has been shown to be well related to the orbital velocity of long waves [Plant et al., 1983]. Thus, the distortion described here is a manifestation of the velocity bunching mechanism described by Alpers and Rufenach [1979]. The width of the spectrum, which in practice is variable, has not been satisfactorily explained to date. Degradation of SAR azimuthal resolution has been attributed both to long wave accelerations [Alpers and Rufenach, 1979] and to scene coherence times [Raney, 1980]. These are essentially explanations of the width of  $\psi(f)$ . Thus, an investigation of the bandwidth of return to a two-scale radar wave probe could shed light on this controversy.

The formulation presented here offers a simple method of simulating SAR performance over the ocean. Using such simulations, variation of SAR parameters— $V/R_0$ ,  $T$ , and  $\Delta V$ —may be easily accomplished by using a single record of output from a two-scale wave probe. To achieve all possible combinations of these parameters in actual SAR experiments would be an expensive, time-consuming procedure. Of course, even in the simulation, changes in environmental conditions can only be obtained by collecting two-scale data under a variety of conditions. Much data of this type have already been collected, however. Similarly, antenna look direction and grazing angle are set at the time the two-scale data are collected. Comparison of simulated images based on these data with SAR images from simultaneous overflights is still necessary to complete validation of the simulation method. Such comparisons are planned for the near future by using MARSEN data.

*Acknowledgments.* The authors appreciate enlightening discussions with Gaspar Valenzuela, Klaus Hasselmann, and Robert Shuchman.

#### REFERENCES

- Alpers, W., Monte Carlo simulations for studying the relationship between ocean wave and synthetic aperture radar image spectra, *J. Geophys. Res.*, **88**, 1745–1759, 1983.
- Alpers, W. R., and C. L. Rufenach, The effect of orbital motions on synthetic aperture radar imagery of ocean waves, *IEEE Trans.*, *AP-27*, 685–690, 1979.
- Alpers, W., and K. Hasselmann, The two-frequency microwave technique for measuring ocean-wave spectra from an airplane or satellite, *Boundary Layer Meteorol.*, **13**, 215–230, 1978.
- Alpers, W. R., D. B. Ross, and C. L. Rufenach, On the detectability of ocean surface waves by real and synthetic aperture radar, *J. Geophys. Res.*, **86**, 6481–6498, 1981.
- Bass, F. G., I. M. Fuks, A. E. Kalmykov, I. E. Ostrovsky, and A. D. Rosenberg, Very high frequency radiowave scattering by a disturbed sea surface, *IEEE Trans.*, *AP-16*, 554–568, 1968.
- Beal, R. C., The SEASAT SAR wind and ocean wave monitoring capabilities, *Rep. JHU/APL SIR 79U-019*, p. 41, The Johns Hopkins Univ., Baltimore, Md., 1979.
- Beal, R. C., D. G. Tilley, and F. M. Monaldo, Large- and small-scale spatial evolution of digitally processed ocean wave spectra from the SEASAT synthetic aperture radar, *J. Geophys. Res.*, **88**, 1761–1778, 1983.
- Gonzalez, F. I., R. C. Beal, W. E. Brown, J. F. R. Gower, D. Lichey, D. B. Ross, C. L. Rufenach, and R. A. Shuchman, Synthetic aperture radar: ocean wave detection capabilities, *Science*, **204**, 1418–1421, 1979.
- Gotwols, B. L., and C. B. Irani, Optical determination of the phase velocity of short gravity waves, *J. Geophys. Res.*, **85**, 3964–3970, 1980.
- Harger, R. O., *Synthetic Aperture Radar Systems*, p. 240, Academic, New York, 1970.
- Harger, R. O., The side-looking radar image of time-variant scenes, *Radio Sci.*, **15**, 749–756, 1980.
- Jain, A., Focussing effects in the synthetic aperture imaging of ocean waves, *Appl. Phys.*, **15**, 323–333, 1978.
- Jain, A., SAR imaging of ocean waves: Theory, *IEEE J. Ocean Eng.*, *OE-6*, 130–139, 1981.
- Larson, T. R., L. I. Moskowitz, and J. W. Wright, A note on SAR imagery of the ocean, *J. Geophys. Res.*, **81**, 2655–2656, 1976.
- McLeish, W., D. Ross, R. A. Shuchman, P. G. Teleki, S. V. Hsiao, O. H. Shemdin, and W. E. Brown, Jr., Synthetic aperture radar imaging of ocean waves: comparison with wave measurements, *J. Geophys. Res.*, **85**, 5003–5011, 1980.
- Peake, W. H., Theory of radar return from terrain, *IRE Nat. Convention Rec.*, **7**, 27–41, 1959.
- Pidgeon, V. W., Time, frequency, and spatial decorrelation of radar sea return, *Memo BPD-670-7*, Johns Hopkins Univ. Appl. Phys. Lab., Baltimore, Md., 1967.
- Plant, W. J., Studies of backscattered sea return with a CW, dual-frequency, X-band radar, *IEEE Trans.*, *AP-25*, 28–36, 1977.
- Plant, W. J., and D. L. Schuler, Remote sensing of the sea surface using one- and two-frequency microwave techniques, *Radio Sci.*, **15**, 605–615, 1980.
- Plant, W. J., W. C. Keller, and J. W. Wright, Modulation of coherent microwave backscatter by shoaling waves, *J. Geophys. Res.*, **83**, 1347–1352, 1978.
- Plant, W. J., W. C. Keller, and A. Cross, Parametric dependence of ocean wave-radar modulation transfer functions, *J. Geophys. Res.*, in press, 1983.
- Raney, R. K., SAR processing of partially coherent phenomena, *Intl. J. Rem. Sensing*, **1**, 29–51, 1980.
- Raney, R. K., Wave orbital velocity, fade, and SAR response to azimuth waves, *IEEE J. Ocean Eng.*, *OE-6*, 140–146, 1981.
- Rice, S. O., Reflection of electromagnetic waves from slightly rough surfaces, *Comm. Pure Appl. Math.*, **4**, 351–378, 1951.
- Rufenach, C. L., and W. R. Alpers, Imaging ocean waves by synthetic aperture radars with long integration times, *IEEE Trans. Antennas Propag.*, *AP-29*, 422–428, 1981.
- Shuchman, R. A., Processing synthetic aperture radar data of ocean waves, in *Oceanography from Space*, edited by J. F. R. Gower, pp. 477–496, Plenum, New York, 1981.
- Shuchman, R. A., A. L. Maffett, and A. Klooster, Jr., Static and dynamic modeling of a SAR imaged ocean scene, *IEEE J. Ocean Eng.*, *OE-6*, 41–49, 1981.
- Swift, C. T., and L. R. Wilson, Synthetic aperture radar imaging of moving ocean waves, *IEEE Trans.*, *AP-27*, 725–729, 1979.
- Tomiyasu, K., Tutorial review of synthetic-aperture radar (SAR) with applications to imaging of the ocean surface, *Proc. IEEE*, **66**, 563–583, 1978.
- Valenzuela, G. R., An asymptotic formulation for SAR images of the dynamical ocean surface, *Radio Sci.*, **15**, 105–114, 1980.
- Valenzuela, G. R., and M. B. Laing, Study of Doppler spectra radar sea echo, *J. Geophys. Res.*, **75**, 551–563, 1970.
- Wright, J. W., Backscattering from capillary waves with application to sea clutter, *IEEE Trans.*, *AP-14*, 749–754, 1966.
- Wright, J. W., A new model for sea clutter, *IEEE Trans.*, *AP-16*, 217–223, 1968.
- Wright, J. W., W. J. Plant, W. C. Keller, and W. L. Jones, Ocean wave-radar modulation transfer functions from the west coast experiment, *J. Geophys. Res.*, **85**, 4957–4966, 1980.

(Received August 17, 1982;  
revised February 7, 1983;  
accepted March 17, 1983.)